# Chapter 4
Diffusion and Transport of Hydrogen

Hydrogen diffusion, tolerating trapping and de-trapping at lattice defects during migration, is expressed by McNabb–Foster equation, Eqs. (2.11) and (2.12). The diffusion coefficient, including tapping parameters, is given in Eq. (2.31). The driving force of diffusion is the concentration gradient, and the diffusion coefficient in the equations is a quantity resulting from the jumping frequency of atoms in a crystalline lattice. The diffusion equation addresses the unit process of the transfer of hydrogen atoms across an atomic plane in a crystalline material and the time change of the hydrogen concentration in a volume element. However, in actual materials, various microstructural inhomogeneities in the diffusion path affect the long-distance transport of a hydrogen atom. Macroscopically observed diffusion coefficients are mostly averaged ones over diffusion paths. This chapter first describes the practice and principles of determining the hydrogen diffusion coefficient. Some factors affecting long-distance hydrogen transport are then presented.

4.1 Determination of Diffusion Coefficient

4.1.1 Diffusion Coefficient Data

Published data on hydrogen diffusion in metals are collected in a book [1], and the range of data for iron and steel is shown in Fig. 4.1 according to the original compilation by McNabb and Foster [2]. A reported value of the hydrogen diffusion coefficient in a 99.99% purity iron specimen, which is almost free from dislocation trapping, is [3]

$$D\left(\mathrm{m^2/s}\right) = 5.8 \times 10^{-8} \exp(-4.5(\mathrm{kJ/mol})/RT). \tag{4.1}$$

77
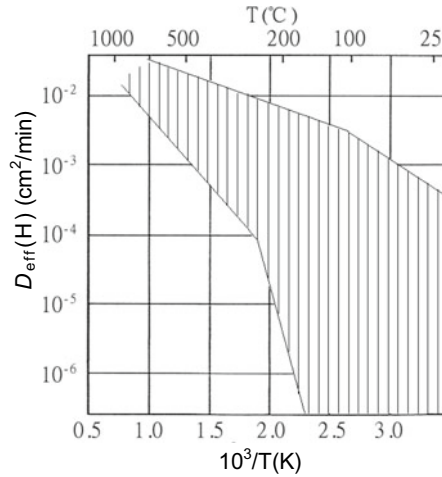
Fig. 4.1 Literature data range of effective diffusion coefficient of hydrogen in iron and steels. Data lines are shown in [2]

The diffusion coefficient in Fick's first law, Eq. (2.1), is a function of temperature. A widespread over three orders of D_{eff} at low temperatures in Fig. 4.1 corresponds to the scatter in the solid solubility shown in Fig. 2.1, resulting from hydrogen trapping at various lattice defects.

Hydrogen atoms migrating in crystalline lattices tolerate various energy barriers. The diffusivity of hydrogen in close-packed fcc γ-iron is lower than that in bcc α-iron due to the higher activation energy of diffusion in fcc structures. Figure 4.2 [4] shows hydrogen diffusion coefficients from the literature in various austenitic stainless steels. The effects of alloying elements on diffusion coefficients are substantial in addition to those of crystal structures. The hydrogen diffusion coefficient reported for Type 304 stainless steel in the temperature range of 311–332 K is [5]

$$D(m^2/s) = 4.41 \times 10^{-7} \exp(-53.5(kJ/mol)/RT). \tag{4.2}$$

Migration distances of hydrogen in terms of $\sqrt{Dt}$ calculated using Eqs. (4.1) and (4.2) at room temperature for α-iron and austenitic stainless steel, roughly 100 μm and 20 nm per second, respectively, are drastically different.

4.1.2 Measurement of Diffusion Coefficient

Hydrogen diffusivity is measured by various methods [6], like gas or electrochemical permeation techniques. Figure 4.3 shows the electrical circuit for the electrochemical cell employed by Devanathan and Stachurski [7]. The specimen is sandwiched
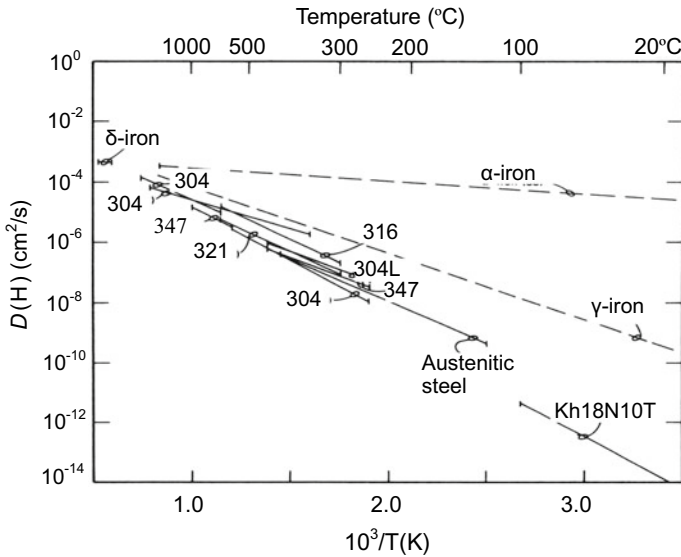
Fig. 4.2 Hydrogen diffusion coefficients in austenitic stainless steel (Caskey [4])

between two individual electrolyte cells, and hydrogen generated electrochemically on one side of the specimen by cathodic polarization is absorbed into the bulk. Then, hydrogen diffusing through the specimen is oxidized at a constant potential. Zero coverage on the opposite side is maintained by anodic polarization, and the oxidation current is proportional to the amount of hydrogen penetrating through the specimen with time. The continuous current record in the anodic potentiostat circuit represents the instantaneous rate of hydrogen permeation.

Figure 4.4 [8] illustrates schematically the permeation transient and its integration with time after the switch-on of galvanostatic cathodic potential. The diffusion coefficient of hydrogen is obtained from the transient curves, but somewhat different quantities are used according to experimental conditions. In the non-steady-state galvanostatic time lag method, a constant hydrogen flux is established at the entrance side by a constant cathodic current. Time lag t_i shown in Fig. 4.4 is expressed from the solution of Fick's second law as [8],

$$t_i = \frac{3 \ln 3}{2} \frac{L^2}{\pi^2 D} \approx \frac{L^2}{6D},$$ (4.3)

where L and D are the thickness of the specimen and the hydrogen diffusion coefficient, respectively.

The integral of the current with time, $\int J dt$, becomes linear when a stationary linear concentration gradient is established in the specimen. Another time lag, t_L, is the time required to obtain a steady-state flow after a sudden change of the boundary condition and is defined as the intercept on the t-axis of the extrapolation of the

Fig. 4.3 Schematic diagram of the electrical circuit for hydrogen permeation experiment (Devanathan et al. [7]. Reprinted with permission from The Royal Society)
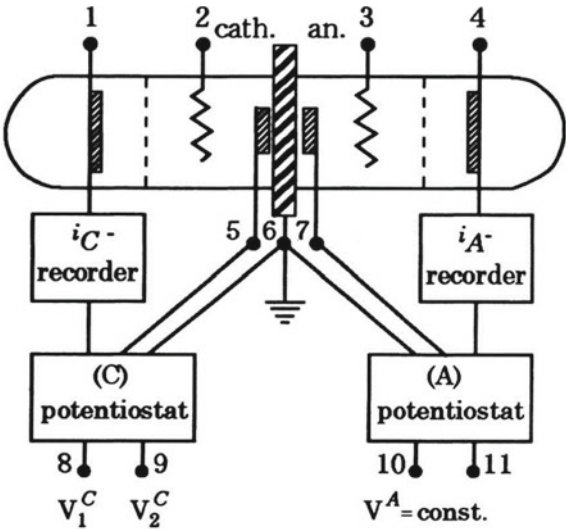
Fig. 4.4 Permeation current density or hydrogen flux J permeating with time after starting galvanostatic cathodic polarization (Boes et al. [8])
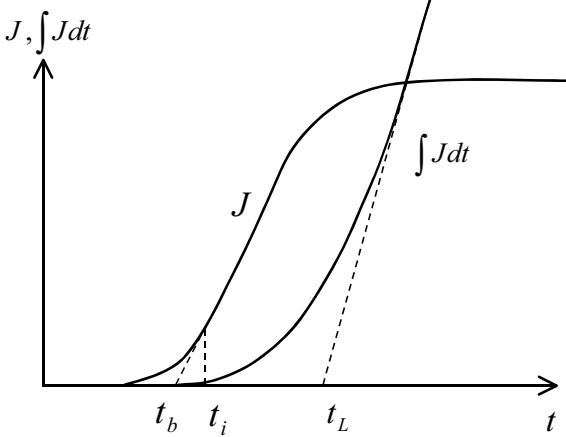
straight line [8],

$$t_{\mathrm{L}} = \frac{L^2}{2D}. \tag{4.4}$$

Further, the break-through time t_{b} is defined as the intersection of the tangent at the inflection point with the initial level $J = 0$,

$$t_{\mathrm{b}} = 0.76\frac{L^2}{\pi^2 D} \approx 0.077\frac{L^2}{D}. \tag{4.5}$$

In the case of the non-steady-state potentiostatic method with a constant hydrogen concentration at the entrance side, expressions for time lag are,

$$t_i = \frac{\ln 16}{3} \frac{L^2}{\pi^2 D} \approx 0.091 \frac{L^2}{D},$$ (4.6)

$$t_L = \frac{L^2}{6D},$$ (4.7)

$$t_b = 0.5 \frac{L^2}{\pi^2 D} \approx 0.05 \frac{L^2}{D}.$$ (4.8)

In this condition, t_L is simply obtained as the time at which the permeation rate is 0.63 of the steady-state value [7].

Determining t_b is not always clear in practice. In electrochemical permeation curves for a high-strength medium-carbon martensitic steel, Frappart et al. defined an apparent diffusion coefficient D_{app} as.

$$D_{app} = \frac{L^2}{Mt},$$ (4.9)

where L and M are, respectively, the sample thickness and a constant depending on the time t chosen in the diffusion transient ($M = 25$, 15.3, 6 for 1%, 10%, 63% J_∞) [9]. Employing D_{app} at a current density of 10% J_∞, Frappart et al. examined D_{app}'s temperature and the cathodic polarization dependencies. Two domains for D_{app} appear, as shown in Fig. 4.5 [9], in the dependence on the subsurface hydrogen concentration C_H estimated using J_∞ and D_{app}. Frappart et al. considered that hydrogen trapping and diffusion compete in domain I, while lattice hydrogen diffusion dominates in domain II, where all trapping sites are filled.

Fig. 4.5 Apparent diffusion coefficient in the Fe–C–Mo high-strength steel as a function of the apparent subsurface concentration of hydrogen at 293 K (Frappart et al. [9])
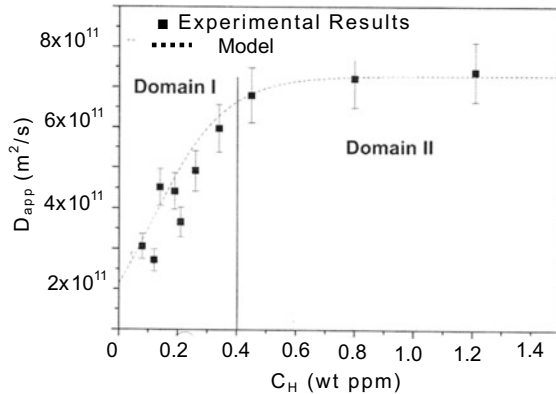
4.1.3 Theoretical Interpretation

McNabb–Foster equation, Eqs. (2.11) and (2.12), describing diffusion accompanying trapping and de-trapping during migration, complements Fick's law that considers the elementary process of atomic jumping. A general solution of the McNabb–Foster equation is complicated, and approximate solutions were derived for thick and thin specimens [2]. The case of thick specimens is described in Sect. 2.2.1.4, and the effective diffusivity is given in Eq. (2.31), including trapping parameters k and p.

McNabb and Foster applied their equation to hydrogen permeation through a plate of thickness L under boundary conditions of constant C_0 and zero hydrogen concentrations on the input and output surfaces, respectively. In the permeation transient in the presence of traps, the time lag t_L required to obtain a steady-state flow was derived in a modified form of Eq. (4.7) as

$$t_L = \frac{L^2}{6D}(1 + \alpha)\left\{1 - \frac{1}{2}\alpha\beta/(1 + \alpha) + O\left(\beta^2\right)\right\}, \tag{4.10}$$

where $\alpha = N_x k/p$, $\beta = C_0 k/p$ [2]. Equations (3.6) and (3.7) are approximated forms of Eq. (4.10). Equation (4.10) is the same form as Eq. (4.7) when the notation of D in Eq. (4.10) is replaced by D_{eff}, defined as

$$D_{\text{eff}} = D(1 + \alpha)^{-1} = D_L\left(1 + N_x\frac{k}{p}\right)^{-1}, \tag{4.11}$$

where N_x denotes the number of trap site per unit volume. Equation (4.11) is the same as Eq. (2.31).

The definitions of p and k express the time required for one trapping or de-trapping event as $1/C_L k$ or $1/p$, while the time to pass through a specimen of the thickness a is a^2/D. "Thick" specimen means frequent trapping and de-trapping events during diffusion through the specimen, i.e., $D/a^2 \ll p, C_L k$. On the other hand, in a "thin" specimen where $D/a^2 \gg p, C_L k$, lattice hydrogen diffuses out readily, and trapping and de-trapping events occur independently. Desorption of hydrogen from a thin specimen then indicates the decrease in the amount of trapped hydrogen controlled by de-trapping, i.e.,

$$\frac{\partial C_x}{\partial t} = -pC_x. \tag{4.12}$$

When thermal equilibrium is established at $t = 0$, the numbers of trapping and de-trapping hydrogen atoms are the same, i.e.,

$$kC_L^0 N_x\left(1 - \theta^0\right) = p\theta^0 N_x, \tag{4.13}$$

where θ denotes the fractional occupancy of the trap. The decrease in trapped hydrogen approximates the amount of remaining hydrogen, which is expressed in terms of trapping parameters as [2],

$$C_x = C_x^0 \exp(-pt) = \theta^0 N_x \exp(-pt) = \frac{C_L^0 N_x k/p}{1 + C_L^0 k/p} \exp(-pt). \qquad (4.14)$$

Casky and Pillinger simulated hydrogen permeation and evolution curves using the finite difference method for a plane sheet to solve the McNabb and Foster equation [10]. The trapping effect was explored for a range of trapping parameter values such as the trap density N, p, and kC. Casky and Pillinger noticed that analysis of the experimental data by the simple time lag or inflection point techniques does not of themselves detect trapping, leading to substantial errors in the calculations of diffusivity and solubility. Casky and Pillinger suggested conducting both permeation and evolution experiments in succession and comparing the two curves.

4.2 Stochastic Theories of Hydrogen Diffusion

The diffusion coefficient has been derived more generally from stochastic viewpoints on the movement of atoms. According to Einstein's relation [11], the mean square displacement of particles is proportional to Dt in Brownian motion. From the viewpoint of random walk, Koiwa assumed that the mean square displacement of a diffusing species after the same number of atomic jumps is the same irrespective of the presence of traps [12]. Since the time of stay at a trap may differ from that at a normal lattice site, the relation between apparent and normal lattice diffusion coefficients is expressed as [12]

$$D_{\text{eff}} t'_{\text{U}} = D_{\text{L}} t_{\text{U}}, \qquad (4.15)$$

where t'_{U} and t_{U} denote the times required for a diffusing atom to make the same number of jumps with and without traps, respectively.

When the saddle point energy change, ΔE, is zero in the energy diagram shown in Fig. 2.13, interstitial atoms visit all sites with an equal probability. In this case, t'_{U} is the weighted mean of the mean stay times at a normal lattice site, t_{L}, and a trap site, t_{T}. Assuming that trap sites for interstitials in the bcc lattice are substitutional foreign atoms of c in atomic ratio, Eq. (4.15) is written for O-occupancy of hydrogen in bcc metals as

$$t'_{\text{U}} = (1 - 2c)t_{\text{L}} + 2c t_{\text{T}}. \qquad (4.16)$$

For T-occupancy of hydrogen, $2c$ in Eq. (4.16) is replaced by $4c$.

The jump frequency ν between the nearest neighbor sites with the activation energy E_a is

$$\nu = \nu_0 \, \exp(-E_a/RT). \tag{4.17}$$

Since the time of stay is the inverse of ν, the form of D_{eff} from Eqs. (4.15)–(4.17) is

$$D_{\text{eff}} = D_L\big[1 - 2c + 2c(\nu_L/\nu_T)\exp(E_b/RT)\big]^{-1}, \tag{4.18}$$

where ν_L and ν_T are frequency factors of the jump from the normal lattice site and trap site, respectively. Equation (4.18) corresponds to Eq. (2.27) derived by Oriani for the case of local equilibrium. Koiwa further considered the case in which the interaction between trapping centers and hydrogen atoms extends to the nearest neighboring sites. In this case, a more general form of D_{eff} was derived, considering a high probability of reverse trapping immediately after the release at the original trap center.

Equation (4.18) is for the case of $\Delta E = 0$ in Fig. 2.13, but it is to be noticed that the saddle point energy substantially affects D_{eff} as shown in Fig. 4.6 [12]. An increase in ΔE, i.e., a decrease in the saddle point energy, increases D_{eff} substantially at low temperatures in the negative curvature range. Surroundings of a defect, like networks, tangles, and cell structures of dislocations, may affect the saddle point energy. In this case, even for traps of the same E_b, the diffusivity of hydrogen affected by dislocations may differ from that in the lattice of low dislocation densities. It is also to be noticed that the assumption of an equal probability for visiting all sites is invalid when $\Delta E \neq 0$.

Fig. 4.6 Effects of the change in saddle point energy ΔE on effective diffusion coefficient of interstitial atoms in the bcc lattice. The straight line shows the normal diffusion coefficient (Koiwa [12])
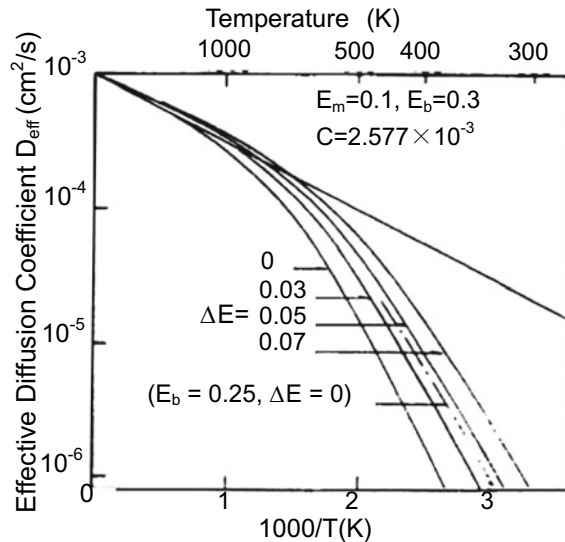
Another stochastic approach to hydrogen diffusion was made by Kirchheim using Monte Carlo methods [13, 14]. The procedure is that interstitial atoms, P in number, are initially distributed randomly in a metal lattice, and each atom is given energy E generated as a random number by the computer. The probability $p(E)$ that an atom has energy E is,

$$p(E) = \exp(-E/RT). \tag{4.19}$$

If the energy E exceeds at least one of the surrounding energy barriers, a jump to a neighboring site is possible, and this step is repeated for a definite number (100 P or 1000 P) of jumps. In the first run during time ^1t, the diffusion coefficient for the ith interstitial atom is calculated in terms of the position vectors $\boldsymbol{R}_i$ and $\boldsymbol{R}_{i0}$ for the final and the initial positions of the ith atom, respectively, as

$$^1D_i = \frac{(\boldsymbol{R}_i - \boldsymbol{R}_{i0})^2}{2d\ ^1t}, \tag{4.20}$$

where d is the dimension of the lattice considered. The ^1D_i is averaged over all P interstitial atoms. Then, the whole procedure is repeated after the time ^kt with the atom, starting from the final position of the previous run until the average of ^1D_i for over all n runs,

$$D = \sum_{k=1}^{n} \frac{^kD\ ^kt}{t}, \tag{4.21}$$

is constant.

The effects of the site and the saddle point energies on diffusion coefficient and site occupancy were examined numerically for the fcc lattice. The calculation results for the effects of the saddle point energy on diffusion coefficient are shown in Fig. 4.7 [13] for dilute solutions, i.e., for low occupancy of the trap. Decreases in both the free energy of a trap site and the saddle point energy reduce the diffusion coefficient compared to the regular lattice, in contrast to Fig. 4.6. It was also shown that the occupancy of a site by an interstitial atom is determined not only by the binding energy in the equilibrium position but also by the heights of surrounding barriers.

Equation 4.18 gives the ratio $D_{\text{eff}}/D_{\text{L}}$. The relation's origin is in Eq. 4.15, i.e., the difference in the jumping frequency or the stay time at the trap and lattice sites. McLellan derived the $D_{\text{eff}}/D_{\text{L}}$ of interstitial solute atoms in defected and defect-free crystals based on the nearest neighbor statistics and the reaction rate theory [15]. Defected crystals contain foreign substitutional atoms, grain boundaries, or dislocations. The calculated form of the ratio was slightly different from Eq. 4.18, though both forms fitted well with experimental data, and discussion was made about the difference [16–18].

Fig. 4.7 Calculated diffusion coefficient in the fcc lattice with traps (1%, $E_t = -20$ kJ/mol) having lower saddle point energies ($\Delta Q = -5$ kJ/mol). The broken line is calculated with $\Delta Q = 0$ (Kirchheim [13])
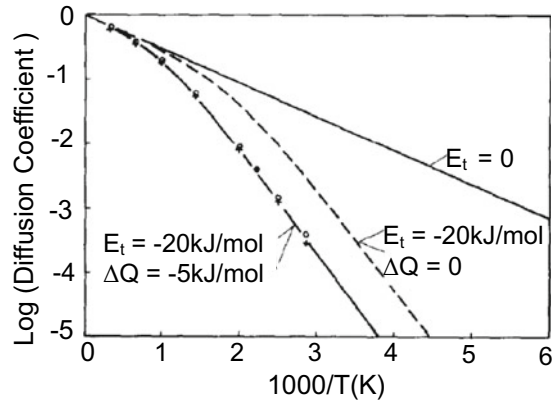
## 4.3 Hydrogen Transport by Moving Dislocations

Fracture in hydrogen embrittlement occurs in most cases under applied strain. Hydrogen transport other than normal diffusion, if any, is a matter to be considered for hydrogen accumulation at a critical site. Hydrogen transport, in addition to diffusion through the lattice, is vital, especially for fcc and hcp metals and alloys in which intrinsic hydrogen diffusivity is low. The drag of hydrogen atoms by moving dislocations is a feasible mechanism, and some observations have been discussed in this respect.

4.3.1 Release of Internal Hydrogen During Straining

Promoted evolutions of precharged tritium during tensile straining are general in various metals and alloys, such as iron, Type 304 stainless steel, nickel, Inconel 718, and 5086 aluminum alloys [19]. In all cases, the release rate increased rapidly at the proportional limit or yield point, reached a maximum with increasing strain, fell with additional strain, and finally showed a significant release at fracture. For iron, the release rate was constant during Lüder's extension, and the rate was a function of temperature and strain rate. Activation energies for the release were about 8 kJ/ and 40 kJ/mol for iron and Type 304 stainless steel, respectively, but the corresponding thermally activated process was not definite.

Similar strain-enhanced desorption of hydrogen was observed for iron and Inconel 625 alloy [20]. A quadrupole mass spectrometer detected hydrogen release during tensile straining of iron specimens. In the experiment, hydrogen was precharged to saturation by cathodic electrolysis, and the test was in a vacuum chamber at room temperature. Figure 4.8(a) shows the hydrogen desorption rate and (b) the stress-time curve for iron [20]. Extraneous hydrogen from dissociated water or molecular hydrogen on the specimen surface was subtracted from the total amount of desorbed
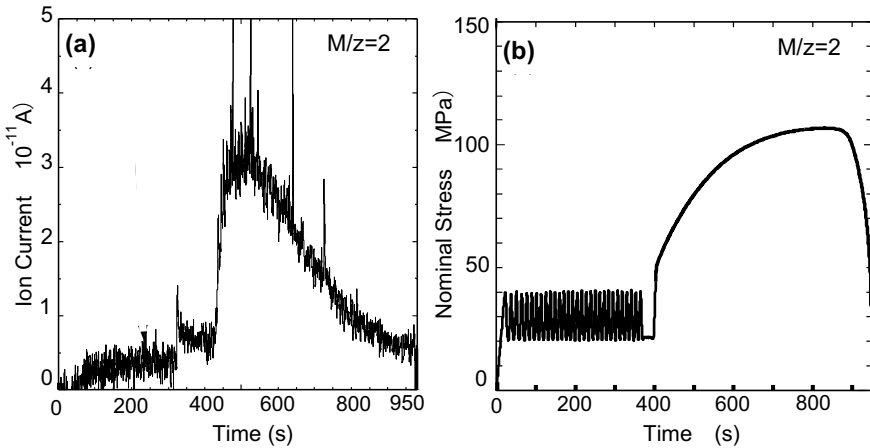
Fig. 4.8 **(a)** Hydrogen desorption during elastic cyclic stressing and subsequent tensile straining until failure of a pure iron specimen. Hydrogen is precharged by cathodic electrolysis in poisoned H_2SO_4 aq of pH 2.5 at a current density of 50 A/m^2. The tensile strain rate is 4.2×10^{-4}/s. The stress-time curve is shown in **(b)** (Shoda et al. [20]. Reprinted with permission from The Iron and Steel Institute Japan)

hydrogen. Cyclic stressing applied in the elastic range prior to tensile straining increased only slightly the desorption rate, but a rapid increase in the early stage of plastic deformation and the subsequent decrease was consistent with previously reported results [19]. The ratio of released hydrogen during tensile straining to the initial content differed by the strain rate. For iron, the ratios were not monotonic against the strain rates in the range from 4.2×10^{-3}/s to 4.2×10^{-5}/s, and the maximum release was 16% at 4.2×10^{-4}/s. On the other hand, for Inconel 625, the fraction of released hydrogen monotonically increased with decreasing strain rate, from almost 0% at 4.2×10^{-3}/s to 9% at 4.2×10^{-6}/s [20].

The hydrogen release from the surface during tensile deformation was directly observed for pure aluminum at different temperatures [21], using the hydrogen micro-print technique described in Sect. 2.3.1. The emission of residual impurity hydrogen during tensile straining to 5% was prominent along coarse slip bands at room temperature, but the emission along grain boundaries, rather than slip bands, was preferential at 355 K. The emission along slip bands was reduced at 203 K. The results at room temperature and 355 K were ascribed respectively to the hydrogen transport by moving dislocations and thermal dissociation of accumulated hydrogen along grain boundaries.

Diffusivities of hydrogen in fcc and hcp metals and alloys are very low at room temperature. Substantial hydrogen desorption implies that the desorption is not simply due to the diffusion of hydrogen but is likely associated with the movement of dislocations. However, the possibility cannot be ruled out that fresh metal surface and/or surface steps formed by slip-off dislocations act as active sites for desorption by reducing the barrier energy for the emission. The prominent tritium

emission at the onset of Lüder's band, shown in Fig. 4.8(a), is most likely due to the evolution of fresh surface on the specimen.

4.3.2 Effects on Electrochemical Permeation

At the steady state of electrochemical permeation, straining of the electrode changes the anodic current. Figure 4.9 [22] is a schematic illustration of anodic current as a function of time when straining is applied to the polycrystalline nickel electrode. Δi_{tot} is the change of the total anodic current by straining, and its magnitude and even the sign differ by materials and experimental conditions.

Various factors affect Δi_{tot}; hydrogen transport by moving dislocations expects an increase in anodic current, but a large portion of Δi_{tot} is the background current to passivate the newly formed electrode surface by straining. The net current Δi_{net} after subtracting the passivation current from Δi_{tot} still includes currents of various origins other than the transport by dislocations, feasibly dynamic trapping by newly created dislocations, an associated depletion of the lattice hydrogen concentration, the decrease in the thickness of the specimen, and the increased input hydrogen concentration by the fresh metal surface enhancing the hydrogen entry. Further, the concentration gradient at the output surface of the specimen is critical to the release of hydrogen diffusing through the lattice. The concentration gradient is not constant at dynamic trapping within the specimen [22].

For polycrystalline nickel electrodes, observed Δi_{tot} was complicated depending on experimental conditions. Δi_{tot} was positive at a strain rate as low as 1×10^{-6}/s
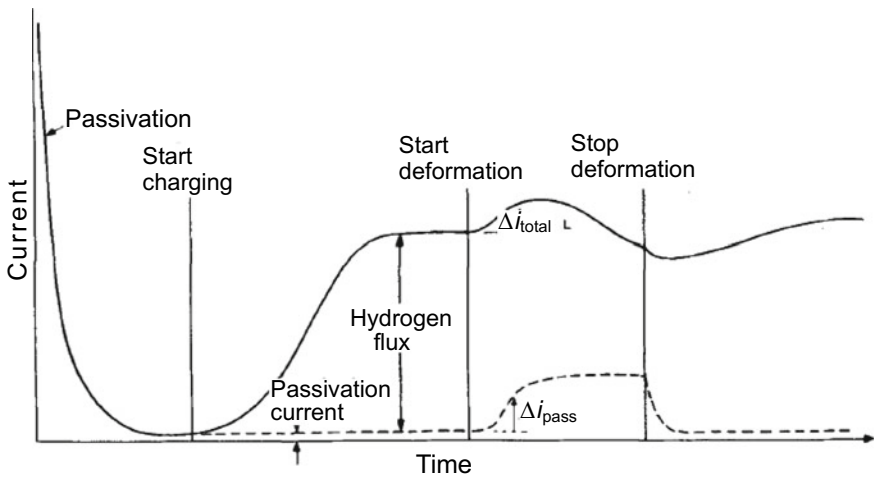
Fig. 4.9 Schematic representation of anodic current for electrochemical permeation through nickel specimen measured as a function of time, illustrating experimental procedure (Frankel et al. [22])

and increased with the amount of strain, but it was negative at strain rates higher than 1×10^{-5}/s [22]. Frankel and Lanision deduced dynamic hydrogen trapping by newly created dislocations, while dislocation transport of hydrogen to great depths is unlikely. However, the specimen for the contribution of the dislocation transport in the easy glide deformation was a thin ($\sim$ 100 μm) single-crystal slice [22]. The passivation current occupied about 90% of the total permeation current [23].

Hydrogen transport by dislocation at electrochemical permeation was also examined for single-crystal iron, concerning the effects of the type of dislocation [24]. Three combinations of the surface orientation and the tensile axis were prepared by slicing specimens of 2 mm in thickness to selectively give the primary slip system for edge, screw, and mixed dislocations, respectively. For all three orientations, applying tensile straining during the steady-state permeation did not affect the anodic current in the elastic range. However, the onset of plastic deformation discontinuously dropped anodic current, reaching nearly constant levels in easy glide regimes. In the strain range of less than 1%, small distinct peaks of anodic current appeared for the screw orientation, but the current fluctuated irregularly around a constant level without showing peaks for edge or mixed orientations.

The decrease in anodic current associated with plastic deformation was mainly ascribed to the trapping of lattice hydrogen by newly generated defects. It was then assumed that hydrogen transport by dislocations gave rise only to small discontinuous peaks for the screw orientation. The increase in hydrogen transport rate per unit strain with decreasing strain rates is consistent with the notion that lattice diffusion of hydrogen, rather than dislocation transport, plays the dominating role in anodic current. Hydrogen transport by moving dislocations was discussed about the hydrogen-carrying capacity, which was dependent on the type of dislocations [24], but definite evidence was not available for dragging hydrogen atoms by moving dislocations.

For polycrystalline iron, electrochemical permeation experiments were conducted using cylindrical specimens of 0.3 mm in wall thickness [25]. Permeation current after subtracting the passivation current is shown in Fig. 4.10 [25] as a function of time from the start of tensile straining during the steady-state permeation stage. The permeation current increased linearly in the elastic range, decreased discontinuously at the onset of plastic deformation, increased gradually, and increased rapidly by stopping the load increase. The discontinuous drop of the permeation current is consistent with a previous study for a single crystal [24] due to the trapping of lattice hydrogen by newly generated defects. Refilling of depleted hydrogen is likely the reason for the following gradual increase and the rapid increase at stopping the load rise. Geometrical thinning of the specimen also caused an increase of permeation current in elastic and also in the plastic ranges.

Fig. 4.10 Change in hydrogen permeation current with elastic and plastic deformation for pure iron (Huang et al. [25]. Reprinted with permission from The Iron and Steel Institute Japan)
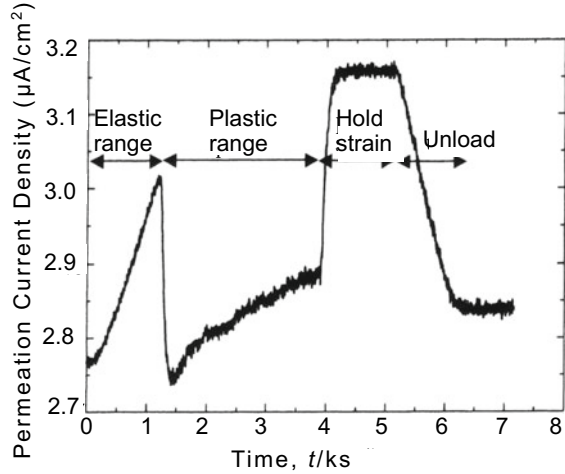
4.3.3 A Kinetic Model

Hydrogen transport by moving dislocations must be affected by increasing dislocation densities during deformation. Charles et al. considered hydrogen transport by dislocations and the trapping process in the apparent hydrogen diffusion. A model assumed was that hydrogen atoms are trapped at dislocations, then transported by dislocations across the sample, and potentially de-trapped to lattice sites. Charles et al. proposed to add a term expressing the time dependence of the trapped hydrogen concentration to the diffusion equation, adopting a model in which plasticity is described using a reaction–diffusion framework [26].

The proposed equation for the density of trapped hydrogen, C_T, was

$$\frac{\partial C_T}{\partial t} = \nabla(D_T \nabla C_T) + \frac{\partial C_T^r}{\partial t}, \tag{4.22}$$

where D_T is the trap (= dislocations) diffusion coefficient. $\partial C_T^r/\partial t$ corresponds to the creation of dislocations. D_T is modified by both strain rate and plasticity. Since the total hydrogen concentration, i.e., the sum of lattice C_L and trapped C_T hydrogen, is constant, the expression of $\partial C_T^r/\partial t$ using the McNabb–Foster equation is

$$\frac{\partial C_T^r}{\partial t} = -\frac{\partial C_L}{\partial t} = \frac{k}{N_L} C_L(N_T - C_T) - pC_T, \tag{4.23}$$

where N_T and N_L are the trap and the normal interstitial lattice site densities, respectively, and k and p are trapping and de-trapping parameters in the McNabb–Foster equation.

Using a finite element method, Charles et al. calculated the hydrogen repartition ahead of the crack tip and the acceleration of the hydrogen transport for various loading conditions and trapping parameters. However, experimental results to be compared were not shown.

4.4   Accelerated Diffusion Along Grain Boundaries

Grain boundaries have two competitional effects on hydrogen transport; one is trapping hydrogen, and another is operating as short paths for diffusion. Hydrogen diffusivities in fcc and hcp metals and alloys are low, but short-circuit effects along grain boundaries are expected to promote hydrogen diffusion. Brass and Chanfreau compared electrochemical permeation curves of commercial high-purity nickel prepared to two grain sizes of 25 and 150 μm polycrystalline samples, 98% cold worked samples, and nickel single crystal [27]. The specimen thickness was 200 μm, giving straight diffusion paths through the sample. Analyses of the diffusion data showed an increase in the diffusion coefficient and the hydrogen flux in the smaller grain size samples of 25 μm, corresponding to short-circuit effects. The estimated intergranular diffusion coefficient was 2–7 times larger than the lattice diffusivity of hydrogen in pure nickel. At an early stage of permeation, the break-through time showed more rapid hydrogen diffusion through the large-grain material.

As a factor operating in grain size effects, intrinsic dislocations accommodating angular misorientations between two grains operate as hydrogen trap sites. Oudriss et al. prepared high-purity polycrystalline nickel specimens of grain sizes ranging from 20 nm to 168 μm [28]. The specimen thickness was 180 μm. Figure 4.11 [28] shows the grain size dependence of the effective diffusion coefficient obtained using the electrochemical permeation technique. The sample preparation methods differ by domains, electrochemical deposition in domain III, and heat treatment for 10 and 150 μm grain sizes in domain II. Oudriss et al. considered the short-circuit diffusion and the hydrogen trapping mechanisms. In domain I, grain boundaries act as a preferential diffusion path. A peak that appeared at a grain size of about 50 μm in Fig. 4.11 was ascribed to the competition between the two mechanisms. The increased density of geometrically necessary dislocations associated with grain refinement likely disturbs hydrogen diffusion. The increase in short-circuit diffusion associated with triple junctions becomes prevalent in nanograin size [28].

On the other hand, permeation tests using polycrystalline high-purity nickel specimens of 10 and 150 μm grain sizes did not provide any evidence supporting enhanced hydrogen transport by grain boundaries [29]. Annealing conditions after cold rolling to prepare the two grain sizes were substantially different, suggesting a difference in intrinsic dislocation densities. Hydrogen diffusion coefficients decrease with decreasing hydrogen concentration in polycrystalline palladium, while it is constant in a single crystal [30]. A reason might be the filling of trap sites formed by dislocations.

Fig. 4.11 Hydrogen
diffusion coefficients in
polycrystalline Ni (Oudriss
et al. [28])
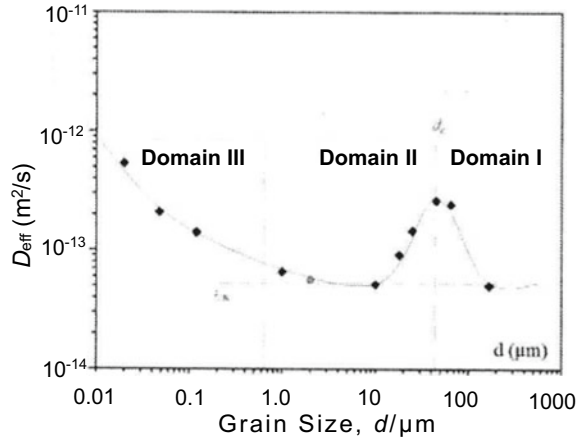
Turnbull and Hutchinson measured hydrogen permeation in duplex stainless steel,
varying the volume fraction of γ-phase by heat treatments [31]. Obtained hydrogen
D_{eff}s decreased with increasing volume fraction of γ-phase, about a factor of 400
less than that for the fully ferritic steel at 44% γ-phase. Turnbull and Hutchinson
deduced that diffusion through the γ-phase has no effect on hydrogen transport and
that the trapping of hydrogen atoms at the α/γ interface is the most significant factor
in reducing diffusivity.

Electrochemical permeation tests are indirect for identifying the grain-boundary
diffusion of hydrogen. Ladna and Birnbaum used secondary-ion mass spectrom-
etry to measure the distribution of deuterium at the surface and grain boundaries of
cathodically deuterium-charged nickel bicrystals [32]. The deuterium concentration
at the grain boundary was higher than in the adjacent grains for high energy 39°
symmetric tilt boundaries ($\Sigma = 9$), while 129° low energy grain boundaries ($\Sigma =
11$) did not have higher D concentration. The diffusivity enhancement along the 39°
grain boundary was about 8 to 17 times, while the diffusivity along the 129° boundary
was equal to the lattice diffusivity in the α solid solution.

Tanaka et al. visualized the distribution of deuterium charged from the surface
of an fcc Fe-30%Ni alloy using Ga-focused ion beam time-of-flight SIMS [33].
Deuterium was enriched in the layer of about 10 μm from the surface, but the
enrichment further proceeded twice or so in depth along grain boundaries, indicating
that grain boundaries can be a fast diffusion path. A more direct dynamic evidence
of hydrogen diffusion along grain boundaries is shown in Fig. 2.19, which observed
permeating deuterium supplied from the bottom of a Type 304 stainless steel spec-
imen [34]. The areas of high deuterium concentration were sites where multiple grain
boundaries were assembled or crossed.

References

1. D.J. Fisher, ed., *Hydrogen Diffusion in Metals—A 30-Year Retrospective* (Scitec Pub., Zürich-Uetikon, Switzerland, 1999)
2. A. McNabb, P.K. Foster, Trans. Metall. Soc. AIME **227**, 618–627 (1963)
3. H. Hagi, Mater. Trans. **35**, 112–117 (1995)
4. G.R. Caskey, Jr., in *Hydrogen Degradation of Ferrous Alloys*, ed. by A. Oriani, J.P. Hirth, M. Smialowski (Noyes Pub., Park Ridge, N. J., 1985), pp. 822–862
5. Y. Sakamoto, H. Katayama, J. Jpn Inst. Metals **46**, 805–814 (1982)
6. P. Kedzierzwawski, in *Hydrogen Degradation of Ferrous Alloys*, ed. by A. Oriani, J.P. Hirth, M. Smialowski (Noyes Pub., Park Ridge, N. J., 1985), pp. 251–270
7. M.A.V. Devanathan, Z. Stachurski, Proc. Roy. Soc. A **270**, 90–103 (1962)
8. N. Boes, H. Züchner, J. Less Common Metals **49**, 223–240 (1976)
9. S. Frappart, X. Feaugas, J. Creus, F. Thebault, L. Delattre, H. Marchebois, J. Phys. Chem. Solids **71**, 1467–1479 (2010)
10. G.R. Caskey Jr., W.L. Pillinger, Metall. Trans. A **6A**, 467–476 (1965)
11. J.L.Bocquet, G. Brebec, Y. Limoge, in *Physical Metallurgy* (vol. 1, 4th Ed) ed. by R.W. Cahn, P. Haasen (Elsevier Sci., Amsterdam, 1996), pp. 536–668
12. M. Koiwa, Acta Metall. **22**, 1259–1268 (1974)
13. R. Kirchheim, Acta Metall. **35**, 271–280 (1987)
14. R. Kirchheim, Prog. Mater. Sci. **32**, 261–325 (1988)
15. R.B. McLellan, Acta Metall. **27**, 1655–1663 (1979)
16. R.B. McLellan, Scripta Metall. **15**, 1251–1253 (1981)
17. D. Farkas, Scripta Metall. **17**, 837–839 (1983)
18. F.D. Fischer, J. Svoboda, E. Kozeschnik, Modell. Simul. Mater. Sci. Eng. **21**, 025008 (2013)
19. J.A. Donovan, Metall. Trans. A. **7A**, 1677–1683 (1976)
20. H. Shoda, H. Suzuki, K. Takai, Y. Hagiwara, ISIJ Int. **50**, 115–123 (2010)
21. K. Koyama, G. Itoh, M. Kanno, J. Jpn. Inst. Metals **42**, 790–795 (1998)
22. G.S. Frankel, R.M. Latanision, Metall. Trans. A **17A**, 861–867 (1986)
23. G.S. Frankel, R.M. Latanision, Metall. Trans. A **17A**, 869–875 (1986)
24. C. Hwang, I.M. Bernstein, Acta Metall. **34**, 1001–1010 (1986)
25. Y. Huang, A. Nakajima, A. Nishikata, T. Tsuru, ISIJ Int. **43**, 548–554 (2003)
26. Y. Charles, J. Mougenot, M. Gaspérini, Int. J. Hydrogen Energy **47**, 13746–13761 (2022)
27. A.M. Brass, A. Chanfreau, Acta Mater. **44**, 3823–3831 (1996)
28. A. Oudriss, J. Creus, J. Bouhattate, C. Savall, B. Peraudeau, X. Feaugas, Scripta Mater. **66**, 37–40 (2012)
29. J. Yao, J.R. Cahoon, Acta Metall. Mater. **39**, 119–126 (1991)
30. T. Mũtschele, R. Kirchheim, Scripta Metall. **21**, 135–140 (1987)
31. A. Turnbull, R.B. Hutchings, Mater. Sci. Eng., A **177**, 161–171 (1994)
32. B. Landna, H.K. Birnbaum, Aeta Metall **35**, 2537–2542 (1987)
33. T. Tanaka, K. Kawakami, S. Hayashi, J. Mater Sci **49**, 3928–3935 (2014)
34. N. Miyauchi, K. Hirata, Y. Murase, H.A. Sakaue, T. Yakabe, A.N. Itakura, T. Gotoh, S. Takagi, Scripta Mater. **144**, 69–73 (2018)